**APPLIED RESEARCH**

# A Dual-Mode FMCW-Doppler Radar With a Frequency Scanning Antenna for River Imaging Applications

**ROBERTO VINCENTI GATTI**[1], **(Member, IEEE),**
**GIORDANO CICIONI**[1], **(Graduate Student Member, IEEE),**
**ALESSANDRO SPIGARELLI**[2], **GIULIA ORECCHINI**[1], **(Member, IEEE),**
**CARLA SALTALIPPI**[3], **AND FEDERICO ALIMENTI**[1], **(Senior Member, IEEE)**
[1]Department of Engineering, University of Perugia, 06125 Perugia, Italy
[2]Elettronica S.p.A., 00131 Rome, Italy
[3]Department of Civil and Environmental Engineering, University of Perugia, 06125 Perugia, Italy

Corresponding author: Giordano Cicioni (giordano.cicioni@dottorandi.unipg.it)

**ABSTRACT** This paper presents a novel frequency modulated continuous wave radar with imaging capability, purposely designed for river monitoring applications. Radar images are obtained using a fixed antenna whose beam can be steered according to the excitation frequency. This is achieved by means of a planar array of slots with a custom feeding network featuring marked frequency squint effects. The radar prototype is experimentally validated in significant scenarios such as those related to static object detection and river water level estimation. The prototype operates in the 24 GHz frequency band and can produce real-time 2D radar maps with a simple signal processing and hardware, the latter implemented in a Raspberry Pi single board computer. The proposed architectures open new prospectives in the field of river monitoring with non-contact sensors, proving how it is possible to properly detect water level, an essential parameter used to estimate the river discharge.

**INDEX TERMS** FMCW radar, frequency beam steering, substrate integrated waveguide (SIW), river monitoring.

## I. INTRODUCTION

River monitoring, and in particular discharge measurement, is essential for effective water management and related services, such as flood protection, irrigation, and hydropower generation. The river discharge can be estimated knowing some main parameters [1]: surface velocity distribution across the river transects, river bathymetry, and water level. Among different methodologies available to determine the surface velocity and water level of rivers, non-contact technologies such as surface velocity radars (SVRs) are particularly appealing, since they can guarantee the safety of

human operations even in dangerous conditions, such as during floods [2]. These types of non-contact sensors can be used in combination with an entropy-based probabilistic model of the river to evaluate the river discharge [3], [4]. The ideal solution to the above problem is based on a system with imaging capabilities both in terms of water level and surface velocity. This can be achieved if the radar can estimate the direction-of-arrival (DoA) and, with this functionality, reconstruct the level/velocity maps.

Historically, DoA estimation was achieved with mechanical beam scanning, by rotating the radar antenna to sweep the beam across the area of interest. Today's market, instead, is populated by compact radar modules that allow the estimation of angular position in both azimuth and elevation by

The associate editor coordinating the review of this manuscript and approving it for publication was Zaharias D. Zaharis.

the use of multiple receivers [5], [6]. Multiple-input multiple-output (MIMO) radars can implement a virtual receiver array with hundreds of elements, for highly accurate DoA estimation [7]. This kind of radar shifts the complexity of the system from the analog radiofrequency frontend (antennas and beamforming network) to the digital domain (analog-to-digital converters (ADCs), memory storage, and signal processing algorithms). It follows that the computational effort needed by these architectures can be excessive for real-time resource-constrained applications, typical of the Internet-of-Things and edge computing scenarios. Besides that, MIMO radars are appealing solutions for monitoring of water flows and surfaces under investigation in recent studies [8], [9].

Active beamforming on the transmitter side is another possibility for DoA estimation in radar sensing. In comparison to mechanical beam steering, active phased array allows rapid beam steering by controlling the phase of each radiating element electronically, with an analog beamformer or fully digitally, [10]. Such an architecture, for example, has been recently adopted in a phased array weather radar system, [11]. Regarding phased array radars, however, analog phase shifters for beamforming networks happen to be costly and limited in both bandwidth and operating frequency.

In the present study, a different architecture for radars with DoA estimation capabilities is explored. This architecture uses the frequency scanning principle [12], [13], [14], [15], [16], [17], i.e. that of a sensor which exploits the enhanced beam squint of the antenna (obtained with a fully passive and non-reconfigurable beamforming network) to perform imaging. By selecting the operating frequency, indeed, the radar beam is focused toward a specific direction on the scan plane, and this allows for DoA estimation keeping a simple single-input single-output (SISO) architecture. For the first time, a radar sensor of this kind is purposely designed for river monitoring applications. The sensor is equipped with two high-gain, substrate integrated waveguide (SIW) slot array antennas in monostatic configuration. These low-sidelobe horizontally polarized antennas, designed with the software SWAN™ [18], feature a 3dB-beamwidth of 6° in azimuth and 9° in elevation. Furthermore, as the transmitter frequency is swept from 23 to 25 GHz, the focused beam scans the environment tilting on the azimuth plane (1D angular estimation) of about ±30°. This enables target detection and imaging capability in the ten meters range with a limited output power. In [19] we already validated the radar sensor in Doppler mode (surface velocity measurements and DoA estimation capabilities) exploiting a flow channel in the hydraulic laboratory of our university. In this paper the system is demonstrated in real-case scenarios in both Doppler and frequency modulated continuous wave (FMCW) modes. Attention is now focused on the precise detection of the target position and of the water level in FMCW mode. Moreover, the radar prototype is demonstrated as SVR in Doppler mode in a river site.

In Section II the hardware and the signal processing of the frequency scanning radar system is described. In Section III-A, the proposed radar prototype is assessed in a static scenario and the results are compared with time-domain simulations. To prove the performance and potentiality of the proposed solution, the radar has been validated in the relevant environment (Sec. III-B) for water level measurements. In Sec. IV are presented, for the first time, the results of the frequency scanning SVR in real case scenario. Sec. V concludes the research and compares the radar sensor with previous studies.

## II. RADAR SENSOR

### A. HARDWARE

The diagram of the frequency beam-steering antenna, the key element of such a system, is shown in Figure 1. As well known [20], [21], the deviation $\theta$ of the beam with respect to the array axis is a function of the frequency $f$, and can be obtained as follows:

$$\theta(f) = \Re e\left[\arccos(\nu)\right] \quad (1)$$

where $\nu = \frac{2\pi}{k_0 d}\left(\frac{\beta L}{2\pi} - \left\lfloor\frac{\beta L}{2\pi}\right\rceil\right)$ with $\nu$ an auxiliary variable introduced to improve equation readability, and the operator $\lfloor\cdot\rceil$ representing the nearest integer function. The parameter $\beta$ is the feeding line phase propagation constant, while $L$ is the length of the delay line between each array element.
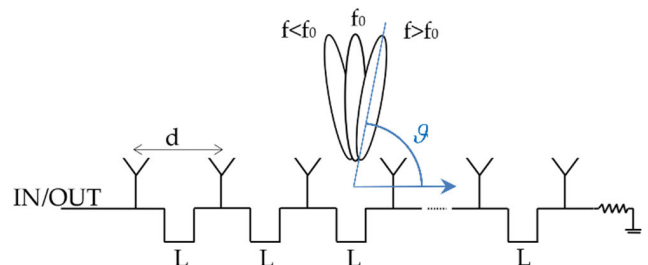


**FIGURE 1.** Travelling-wave array antenna of radiating elements, spaced by a distance *d* and connected in series by delay lines of length *L*.

The parameter $\nu$ can be derived as follows:

$$\nu_m = \frac{\lambda}{d}\left(\frac{\lambda_{g_0}}{\lambda_g}n - m\right), m \in \mathbb{N} \quad (2)$$

and

$$\nu = \nu_{\bar{m}} \quad (3)$$

with $\bar{m}$ such that

$$|\nu_{\bar{m}}| = \min_m |\nu_m| \quad (4)$$

In Figure 2 the pointing angles of a frequency beam-steering antenna with a central frequency of 24 GHz are depicted for various values of $n$. For each given frequency range, an optimal value of the parameter $n$ can be identified such that the angular range scanned by the radar is maximized.

As shown in Figure 2, if the length of the delay lines is increased (by increasing the parameter $n$), it is possible to span approximately the same field of view with a smaller bandwidth (i.e., frequency range transmitted by the radar).
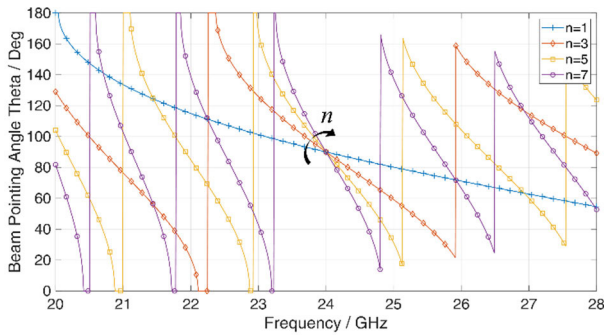
**FIGURE 2.** Array pointing angle vs. transmitted frequency. This graph shows the beam frequency squint of the radar antenna, an effect that is used to create radar images.

When the frequency is close to the central frequency $f_0$, it can be verified that the required value of the parameter $m$ is $m = n$. Near $f_0$, (1) becomes:

$$\theta(f) = \arccos\left[n\frac{\lambda}{d}\left(\frac{\lambda_{g0}}{\lambda_g} - 1\right)\right] \tag{5}$$

The above equation allows to find the optimal value of $n$, and therefore the optimal delay lines length $L$, required to obtain the desired field of view for a given bandwidth. The manufactured antennas are designed choosing $n = 3$.

The implemented prototype (shown in Figure 3, from [19]) is based on the Infineon BGT24MTR11 radar transceiver (TRX) and on the Analog Devices ADF4158 phased-locked loop (PLL), that is used as frequency synthesizer (block diagram in Figure 4, from [19]). The power at the input of the transmitting antenna is 9 dBm. The single sideband (SSB) noise figure (NF) of the receiver is 12 dB. The in-phase/quadrature (I/Q) outputs of the homodyne receiver are amplified and filtered by a low-frequency operational amplifier stage (IF stage in Figure 4). Two versions of the IF stage are implemented, selected depending on the operative mode of the sensor: FMCW mode in Figure 5 and Doppler mode in Figure 6. The FMCW IF stage is designed to remove the low-frequency components due to the coupling between the TX and RX antenna. Moreover, its voltage gain
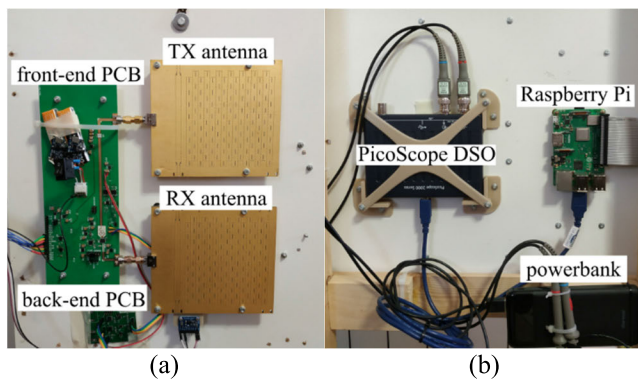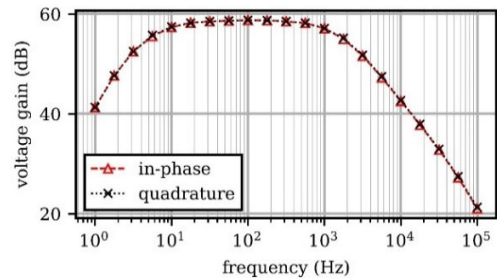


**FIGURE 3.** Radar prototype: (a) front view and (b) back view.
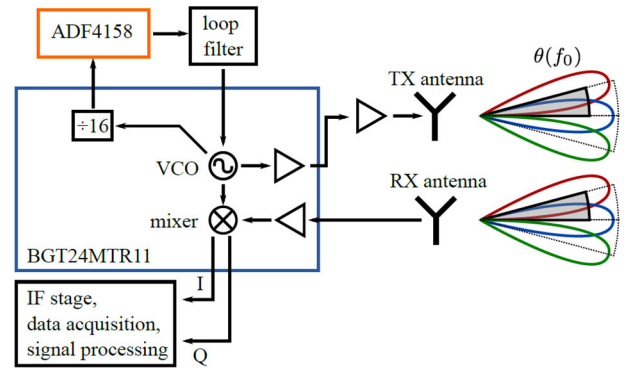


**FIGURE 4.** Block diagram of the radar prototype.
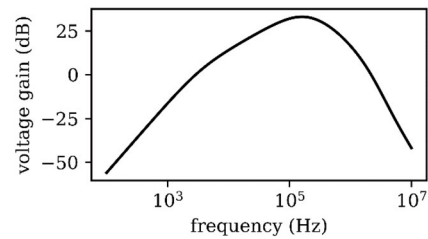


**FIGURE 5.** Voltage gain of the IF amplification and filtering stage in FMCW mode.



**FIGURE 6.** Voltage gain of the IF amplification and filtering stage in doppler mode.

is maximized for farthest distances and increases gradually to avoid the amplifier saturation in presence of near targets, which corresponds to lower beat frequencies. The Doppler IF stage is designed to remove the residual DC components of the signal and to limit the bandwidth in the frequency range of interest for SVR application. The I/Q outputs are acquired and processed in real-time by a single-board computer (Raspberry Pi) on board the radar system, that is battery-powered and controlled wirelessly.

The antenna beam varies its direction from $-33°$ at 23 GHz to $+35°$ at 25 GHz. The radiation diagram of these antennas has been previously published in [19]. Since the steering capabilities of the antenna beam with frequency are essential to correctly reconstruct and interpret the radar images, the antenna is characterized as follows. First the azimuth angle of the beam is experimentally determined for a discrete set of frequency points, then a linear model is best fitted to
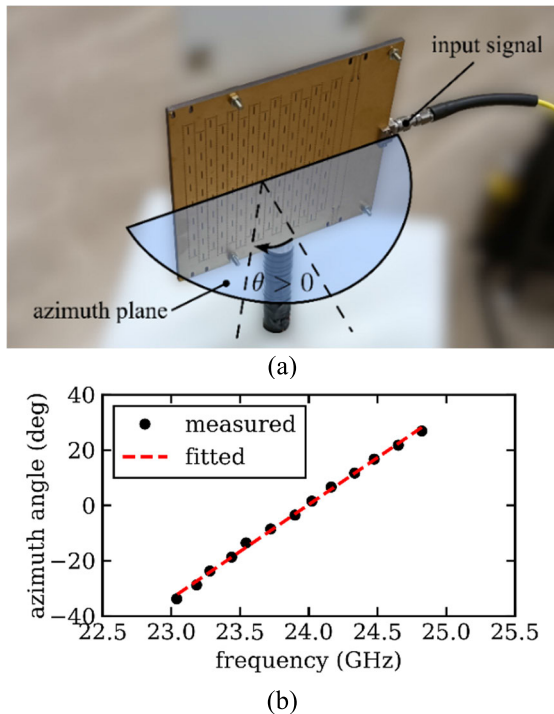
**FIGURE 7.** Measurement setup (a) for beam steering angle vs. frequency characteristic (b). The equation describing pointing angle ($\theta$, in degrees) versus the operating frequency ($f_{GHz}$, in GHz), is given by the following fitted expression: $\theta = 34.0 \cdot f_{GHz} - 814.6$.

the measurements, as shown in Figure 7. The linear fitting approximates the inverse cosine function of Eq. (1), that holds valid considering the value of $n = 3$ of Eq. (2), and the angular and range resolutions of the radar system.

### B. SIGNAL PROCESSING
The signal processing algorithm can be applied to both simulated and measured time-domain signals, and consists in the following main steps:

1) STFT of the I/Q signal.
2) time-angle mapping.
3) IF-stage voltage gain compensation.
4) antenna gain compensation.
5) free-space losses compensation.

The STFT produces a spectrogram, a time-vs-frequency image. Since the beam direction is a one-to-one function of frequency, and since the frequency is a function of time, according to the modulation used (e.g., linear ramp), the time axis of the spectrogram can be mapped into angular position. This held true considering that the time required for the radar to scan the entire Field-of-View (FOV) is significantly larger than the round-trip time of the transmitted radar signal.

To obtain the final radar image, the spectrogram is represented in a Cartesian coordinate system. Several post-processing equalization steps on the spectrogram can be performed, to make the amplitudes of the spectrogram peaks proportional to the radar cross section (RCS) of the targets. In particular, the post-processing steps consider that the

voltage gain of the IF amplification stage is not constant over frequency; the realized gain of the antenna is not constant over the pointing angle; free-space losses occur.

### III. RESULTS IN FMCW MODE
Two experiments are presented in this section. In the first, the radar is used to sense a static scenario, with several targets at different ranges and angular positions. In the second experiment, the radar is used to measure the distance of the radar from the surface level of a river.

In the experiments described in this section, the radar frequency synthesizer was programmed to produce a linear ramp (upchirp time 6ms, bandwidth 2GHz, start frequency 23GHz). With these settings, an object at 1-m distance results in a beat frequency of 4.4kHz. The I/Q receiver outputs are acquired at a sampling frequency 10MHz with a Pico-Scope 2206B USB oscilloscope. The upchirp time is chosen to guarantee that the beat frequencies corresponding to the targets fall inside the useful bandwidth of the low-frequency amplification stage.

### A. STATIC SCENARIO
The radar is used to detect several objects in the courtyard of the Department of Engineering, in Perugia, Italy (top view in Figure 8). The sensor is placed in vertical position at a height of 70 cm from the ground, at one side of the courtyard. In this way, the radar scans the environment horizontally. Several objects are in the scenario, such as streetlights, trees, and buildings on the perimeter of the courtyard. The closest object is a streetlight at 18 m, while the farthest is the building at 71 m.
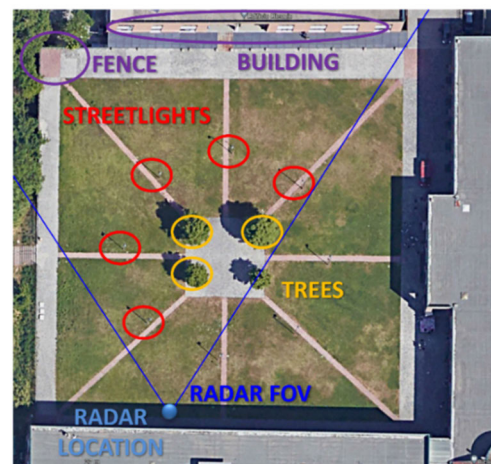


**FIGURE 8.** Top view of the scenario observed with the radar. In the courtyard, there are several streetlights, trees, and buildings along the perimeter. GPS location: 43°07′07.2″N 12°21′19.8″E.

Figure 9 shows that all the main targets in the FOV of the radar are correctly detected, in both range and angular position. The intensity of the dots on the radar image is higher for metallic targets (streetlights) and lower for other targets, such as trees. The only exception is the streetlight at the right
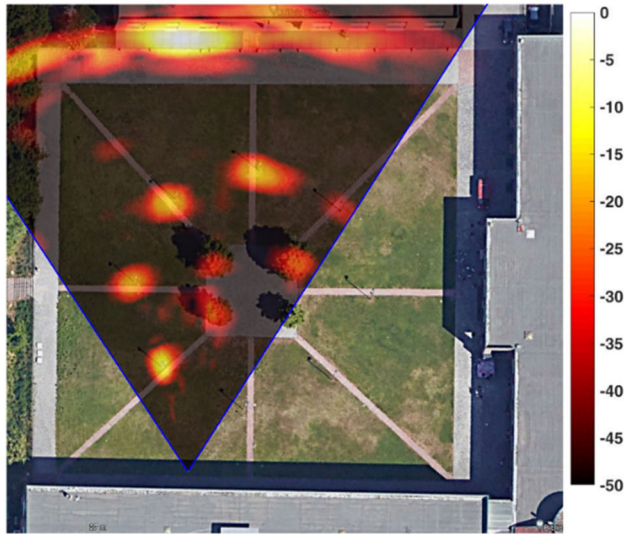
**FIGURE 9.** Radar image overlayed with satellite image of the scenario. The color scale represents the normalized STFT magnitude, in dB.

**TABLE 1.** Target list.

| Target | Distance (m) | Angle (deg) | $RCS/ \min(RCS)$ |
|---|---|---|---|
| streetlight | 18.2 | -8.9 | 10 |
| streetlight | 32.4 | -13.3 | 10 |
| streetlight | 44.7 | -1.3 | 10 |
| streetlight | 50.6 | 15.1 | 10 |
| streetlight | 49.2 | 34.7 | 10 |
| tree | 26.6 | 9.7 | 1 |
| tree | 34.3 | 9.3 | 1 |
| tree | 38.2 | 30.6 | 1 |
| building | 71.8 | 1.5 | 500 |
| building | 71.4 | -8.9 | 20 |
| building | 77.0 | 12.1 | 50 |
| building | 74.3 | 15.1 | 20 |
| building | 74.6 | 20.9 | 20 |
| fence | 72.7 | -18.9 | 20 |
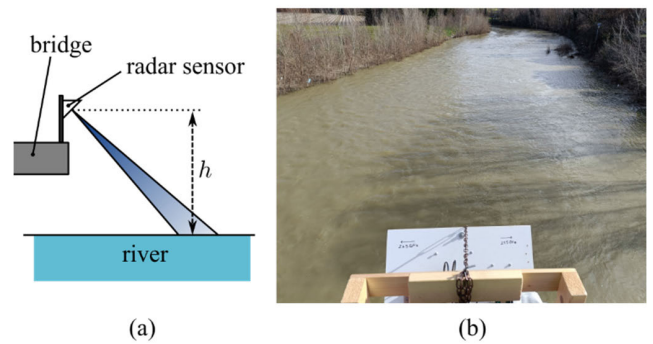


**FIGURE 11.** Radar measurements of water level on Tiber River (43°00′36.8″N 12°25′45.3″E, 28/02/2023 10:30 AM): (a) illustration of experimental setup and (b) photograph from radar point-of-view.

edge of the radar FOV, that is less intense in the radar image since it is aligned with one of the trees. The building in front of the radar at a 71 m distance is correctly detected as well. The radar image is reproduced with simulation, as shown in Figure 10. The target position and their (estimated) RCSs are summarized in Table 1, where the RCS of each single target is normalized with respect to the minimum RCS, which is estimated to be 0.01 m$^2$.
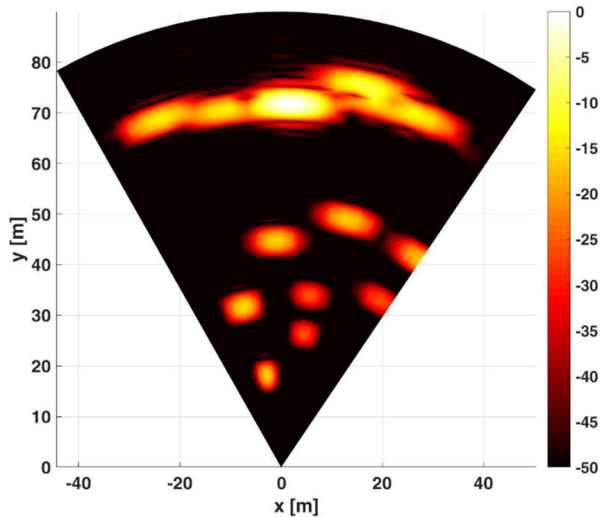


**FIGURE 10.** Radar image obtained from simulation. The color scale represents the normalized STFT magnitude, in dB.

### B. RIVER WATER LEVEL

After the validation in static scenario of both simulation software and radar prototype, the sensor is used to detect the water level of Tiber River in Ponte Nuovo, Perugia, Italy (setup shown in Figure 11). The radar is placed on the bridge

above the river, with a tilt angle of 45°. The information about the water level obtained with the radar is compared with benchmark data from the monitoring infrastructure already present (ultrasonic level sensor). At the time of the experiment, the water level is 2.37 m over the hydrometric zero (162.04 m above the sea level), which corresponds to a vertical distance between the radar and the water level $h = 10.19$ m. In Figure 12 it is shown the radar image obtained from measurements. The peak of the spectrogram corresponds to the moment in which the radar beam is aligned with the water flow, where the backscattered power is maximized. The radial distance between the river surface and the radar (14.6 m) is in agreement with the height of the water and the tilt angle of the sensor. In terms of angular position, the main peak in the spectrogram is placed at an angle of +10°. This can be interpreted considering that the radar is mounted on the fence of the bridge, which is not exactly perpendicular with the river flow. The pattern due to the signal reflected by the surface of the river is replicated at double the distance (i.e., at about 28 m). An explanation for this effect is that the radar metal parts, the antennas, act as a reflector for the signal backscattered by the river. In this way, the river surface appears twice in the radar image. In Figure 13 it is possible to see the radar image on the X-Y plane of the radar
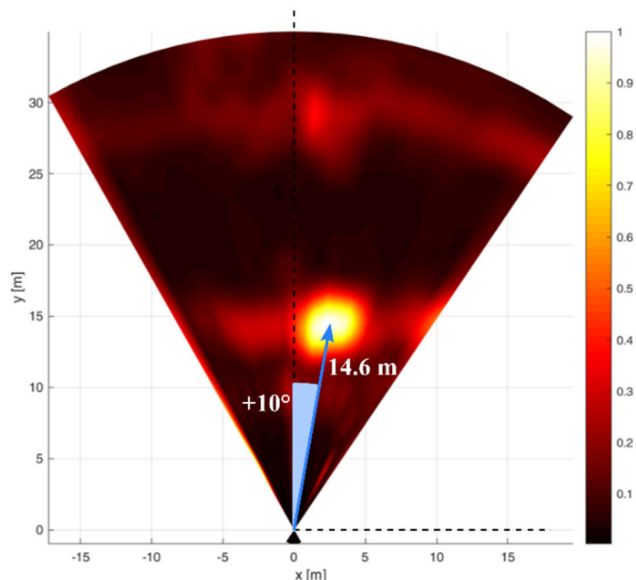
**FIGURE 12.** Radar image obtained measuring water level of Tiber River. The color scale represents the normalized STFT magnitude, in linear scale.
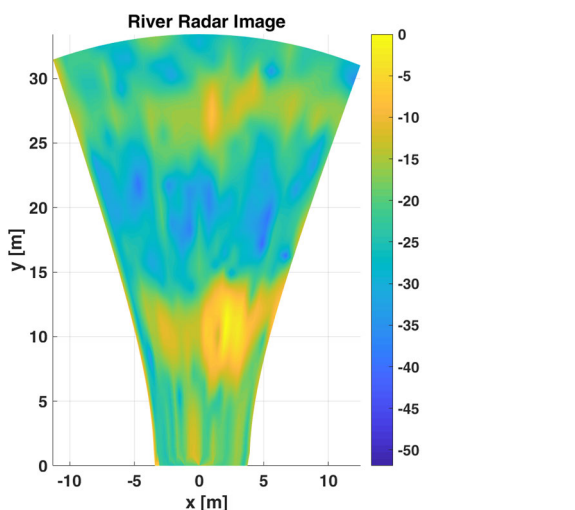


**FIGURE 13.** Radar image mapped on river surface. The color scale represents the normalized STFT magnitude, in dB.

reference system (azimuthal plane) but projected on a plane in the river's X-Y-Z Cartesian coordinate system, where Z is constant and so that the plane represents the river surface. This projected image is obtained as explained in Appendix B. This kind of image highlights the area of the river illuminated by the radar during the measurements.

## IV. RESULTS IN DOPPLER MODE

Understanding river discharge is crucial in river monitoring, and the surface velocity across transects is valuable for its assessment [4]. For this reason, the proposed radar is assessed also as SVR in river scenario. Two experiments are performed. First, the radar is used for horizontal scanning, while the second experiment is for vertical scanning. The setup and

the river site position are the ones described in Figure 11, with the difference that the measurements have been taken approximately one month in advance (18 January 2023, 11:00 AM), in occurrence of a high flow event. In this event, the vertical distance between the radar and the river surface was $h = 5.93$ m (water level 168.67 m.a.s.l.).

To evaluate the surface velocity, several angles must be considered:

- Heading of the river, $\phi_{river}$: angle between the geographical North direction and the flow direction (clockwise).
- Heading of the radar, $\phi_{radar}$: angle between the geographical North direction and the broadside direction of the radar (clockwise).
- Beam deviation with respect to the broadside direction of the radar, $\theta_{dev}$ (clockwise).
- Tilt angle of the sensor, $\theta_{tilt}$.

The beam deviation angle is $\theta_{dev}(f) = 34.0 \cdot f_{GHz} - 814.6$, as described in Figure 7.

### A. HORIZONTAL SCAN

The radar is synchronized in five operating frequencies ranging from 23.5 GHz to 24.5 GHz, to measure the surface velocity on five points across throughout the river width. For each direction, an acquisition of 1 second is performed, with sampling frequency 100 kHz. With the same signal processing described in [19], the sampled I/Q signals are recombined in complex form, high-pass filtered digitally, and then the fast Fourier transform (FFT) is evaluated, and the properties of the Doppler centroid corresponding to the moving river surface are estimated (bandwidth and center frequency). An example of acquisition is shown in Figure 14.
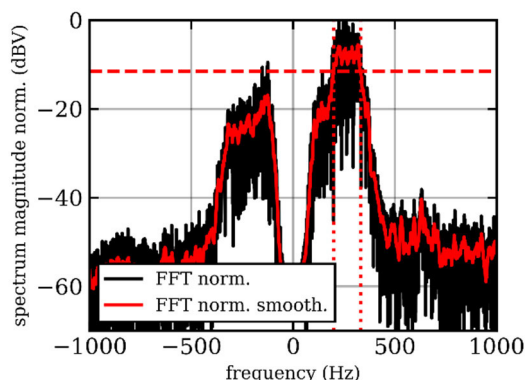


**FIGURE 14.** Horizontal scan, acquisition corresponding to the operating frequency of 23.5 GHz. The Doppler centroid is centered at 264.4 Hz and has a 6-dB bandwidth of 132.8 Hz. In black the FFT evaluated with 0.1 Hz resolution, and in red the smoothed version with moving average, evaluated before the estimation of the Doppler centroid parameters.

The radar detects the radial component of the velocity $v_r$, that is proportional to the center frequency of the Doppler centroid. The surface velocity $v$ in the direction of the flow can be obtained with the following equation:

$$v = \frac{v_r}{\cos \theta_{tilt} |\cos(\phi_{river} - \phi_{radar} + \theta_{dev}(f))|} \quad (6)$$

where $\theta_{tilt} = -45°$, $\phi_{river} = 240°$, and $\phi_{radar} = 50°$. The denominator of Eq. (6) is a scaling factor for the radial velocity $v_r$ due do the angle of observation of the radar. The results of the horizontal scan are reported in Table 2, while Figure 15 represents the surface velocity values and their position on the transect. In the fourth column is reported the value of the scaling factor, that changes for each beam deviation angle. The surface velocity corresponding to the operating frequency of 24.5 GHz is not detected, because no Doppler centroid is found on the spectrum. Further investigation is needed to establish the cause of this effect, but it is reasonable to consider as the primary cause the angle of observation being over a certain maximum value.

**TABLE 2.** Horizontal scan results.

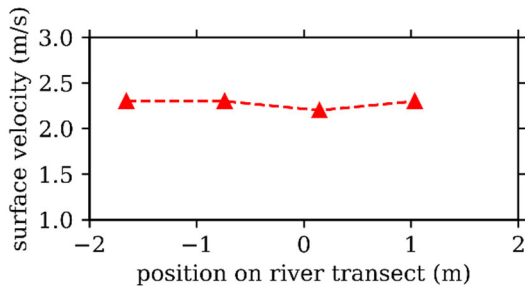| Frequency (GHz) | Beam deviation from broadside $\theta$ (deg) | Doppler Centroid center frequency (Hz) | Scaling factor | Surface velocity (m/s) |
|---|---|---|---|---|
| 23.50 | -15.6 | 264.4 | 1.421 | 2.3 |
| 23.75 | -7.1 | 256.9 | 1.416 | 2.3 |
| 24.00 | +1.4 | 247.1 | 1.443 | 2.2 |
| 24.25 | +9.9 | 246.6 | 1.504 | 2.3 |
| 24.50 | +18.4 | - | 1.608 | - |



**FIGURE 15.** Surface velocity profile. The position on the river transect is evaluated from the tilt angle of the sensor ($\theta_{tilt} = -45°$), the beam deviation angle ($\theta$), and the height of the radar from the water level ($h = 5.1$ m). The position zero meters corresponds to $\theta = 0°$, which is when the radar points broadside.

### B. VERTICAL SCAN
In this experiment the radar has been rotated by 90°, so that the scan plane of the antenna is vertical. Varying the radar operating frequency from 23.5 GHz to 24.5 GHz, the direction of observation of the radar changes, elevating the beam and looking at the river surface at a farther distance. The purpose of this experiment is to verify that surface velocity values obtained on different elevations are in agreement.

The surface velocity $v$ in the direction of the flow can be obtained with the following equation:

$$v = \frac{v_r}{\cos(\theta_{tilt} + \theta_{dev}(f))|\cos(\phi_{river} - \phi_{radar})|} \quad (7)$$

where $\theta_{tilt} = -40°$, $\phi_{river} = 240°$, and $\phi_{radar} = 50°$. The results of the vertical scan procedure are reported in Table 3 and in Figure 16. In Figure 17 the comparison between the

**TABLE 3.** Vertical scan results.

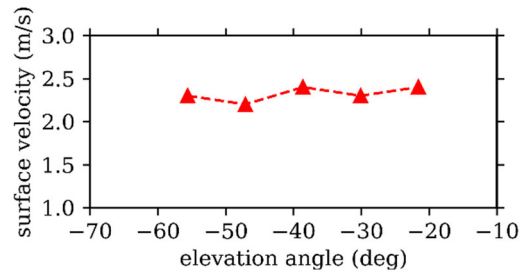| Frequency (GHz) | Beam deviation from broadside $\theta$ (deg) | Doppler Centroid center frequency (Hz) | Scaling factor | Surface velocity (m/s) |
|---|---|---|---|---|
| 23.50 | -15.6 | 197.3 | 1.797 | 2.3 |
| 23.75 | -7.1 | 234.4 | 1.492 | 2.2 |
| 24.00 | +1.4 | 292.0 | 1.299 | 2.4 |
| 24.25 | +9.9 | 316.6 | 1.174 | 2.3 |
| 24.50 | +18.4 | 346.5 | 1.092 | 2.4 |



**FIGURE 16.** Surface velocity values obtained from vertical scan. Changing the beam deviation angle, the surface velocity is evaluated for several elevation angles $\theta_{tilt} + \theta_{dev}(f)$. The values are in agreement.
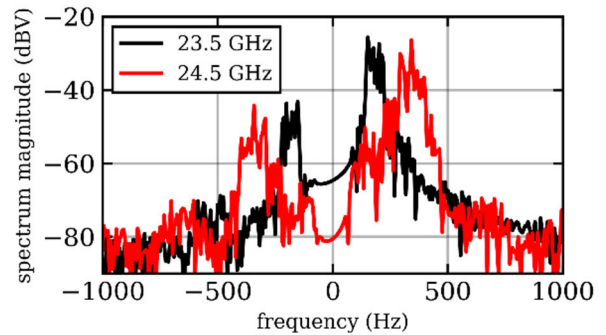


**FIGURE 17.** Vertical scan, acquisitions corresponding to the operating frequencies of 23.5 GHz (black) and 24.5 GHz (red). For this experimental setup, the higher the operating frequency, the lower the beam deviation, the higher the radial component of the surface velocity, the higher the central frequency of the Doppler centroid.

spectra of the I/Q complex signal at the extremes of the angular scanning range is shown. The surface velocity values are in agreement, also with the horizontal scan.

## V. DISCUSSION
A comparison of this sensor with previous works concerning FMCW frequency scanning radars is presented in Table 4. To detect the water from a far distance a tailored frequency scanning planar array antenna in SIW technology with focused beam in both azimuth end elevation is designed. To the authors' knowledge, this work presents the first FMCW radar sensor with frequency scanning planar array antenna in SIW technology. This design choice enables the detection of far targets with low transmit power, with a demonstrated maximum distance of 80 m. Moreover, this work presents the first radar with frequency scanning antenna

**TABLE 4.** State-of-the-art for FMCW radar sensors with frequency scanning antenna.

| Ref. | Operative Frequency (GHz) | Mode | Array geometry | Beamforming network technology | Radiating element | Angular scan interval | Power @ TX antenna (dBm) | Max detection range achieved (m) | HPBW |
|---|---|---|---|---|---|---|---|---|---|
| [12] | 24 | FMCW | linear | rectangular waveguide | open waveguide | 49° | n.a. | 40 | 10° × n.a. |
| [14] | 16.5 | FMCW | linear | microstrip | patch | 32° | n.a. | 2 | 8° × n.a. |
| [15] | 60 | FMCW | linear | SIW | slot | 60° | n.a. | 8 | 6° × n.a. |
| [16] | 60 | FMCW | linear | SIW | slot | 60° | n.a. | 10 | 6° × 120° |
| this work | 24 | FMCW & Doppler | planar | SIW | slot | 60° | 9 | 80 | 6° × 9° |

capable of dual-mode operation (i.e., FMCW and Doppler modes), and the first time such a radar architecture is used in river monitoring application, for the evaluation of the water level and the surface velocity distribution across the river width.

## VI. CONCLUSION

In this paper an FMCW frequency scanning radar has been demonstrated, for the first time, for river monitoring applications. The radar prototype operating at 24 GHz is realized and the system is assessed in two real-case situations. In the first case the courtyard of the Department of Engineering is considered, and all the static targets were correctly detected. Simulations of the same scenario are compared with measurements data, and the two agree. In the second case, instead, a real river scenario is considered, and the radar was capable of correctly measuring the water level, producing, in the meantime, images of the river surface. After that, the radar prototype is demonstrated as SVR in real case scenario for the first time.

The obtained results, although preliminary, show that the proposed architecture opens new possibilities in the field of river monitoring by means of non-contact sensors. The minimal signal processing effort required by the radar, along with its imaging capability, indeed, makes it appealing for real-time edge-computing applications.

Future works include the development of signal processing algorithms to estimate surface velocity radar maps directly from the acquisitions in FMCW mode. Together with the water level, such a parameter is essential for assessing river discharge.

## APPENDIX A
## MODELING OF THE FMCW RADAR SYSTEM

To carry out time-domain simulations of the radar system, a simulation software has been developed. This tool allows optimal dimensioning of the FMCW frequency scanning radar system, by evaluating the radar performance for an arbitrary antenna geometry, bandwidth, modulation frequency, etc. The simulation considers non-idealities such as Additive White Gaussian Noise (AWGN) noise on signals, coupling effects between transmitting and receiving antennas, ADC quantization noise, and waveguide dispersion effects.

The simulation software produces the radar received signal in the time domain. Fast Fourier Transform (FFT) and Short Time Fourier Transform (STFT) are used to provide radar images from the resulting time domain signals.

More in detail, the software simulates the propagation of the signals through the antenna and calculates the received signal from the contributions due to each radiating element. Given an arbitrary set of targets, with polar coordinates $(R_i, \psi_i)$ as shown in Figure 18, all the paths from each transmitting radiating element to each receiving element of the array are derived and combined with the proper time delays and amplitudes. The scenario is represented by $M$ targets placed on the scanning plane of the array antenna, each described in terms of its radial distance $R_i$ from the radar, angular position $\psi_i$ and RCS $\sigma_i$. The parameter $P_{i,j}$ is the distance between the $j$-th transmitting element and the $i$-th target.
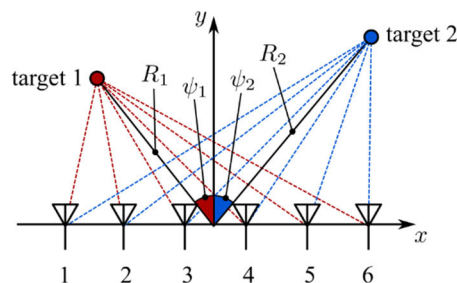


**FIGURE 18.** Analysis scenario with multiple targets on the scanning plane of the array antenna. The $i$-th target is located at $(R_i, \psi_i)$, expressed in polar coordinates.

With reference to Figure 18, this set of data is arranged in matrix form as follows:

$$P == \left\{ \left[ (\boldsymbol{R} \circ \sin \boldsymbol{\psi})^T \boldsymbol{J}_{1,N} - d\boldsymbol{J}_{M,1} \left( \begin{bmatrix} 1 & 2 & \cdots & N \end{bmatrix} \right. \right. \right.$$
$$\left. \left. \left. - \frac{N+1}{2} \right) \right]^{\circ 2} + \left[ (\boldsymbol{R} \circ \cos \boldsymbol{\psi})^T \boldsymbol{J}_{1,N} \right]^{\circ 2} \right\}^{\circ \frac{1}{2}} \quad (8)$$

where the matrix row index is associated with the target, the matrix column index with the radiating element, the symbol ∘ is the Hadamard operator, while $J_{M,N}$ indicates an $M \times N$ matrix of ones. For each considered forward path toward a

given target $i$, the associated backscattering produces $N$ different signals, directly related to $N$ different return paths $P_{i,j}$, as shown in Figure 19.
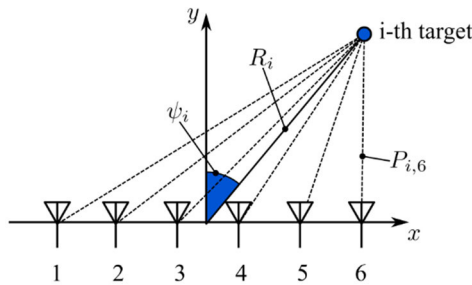


**FIGURE 19.** Return paths associated with a generic target, with $N = 6$.

For each path $P_{i,j}$, the associated time of flight can be calculated as follows:

$$t_{r_{ij}} = \frac{P_{i,j}}{c_0}. \tag{9}$$

The FMCW beat signal is typically derived as follows:

$$b_1(t) = \cos[2\pi f(t)t - 2\pi f(t - t_R)t] \tag{10}$$

where $f(t)$ is the instantaneous transmitted frequency and $f(t - t_R)$ is the instantaneous received frequency, with $t_R$ representing the round-trip time of the signal [22]. Since for a single-ramp chirp signal the instantaneous frequency corresponds to:

$$f(t) = f_0 + \Delta f f_m t \tag{11}$$

from (10) and (11) follows:

$$b_1(t) = \cos[2\pi \Delta f f_m t_R t] \tag{12}$$

where $f_m$ is the chirp modulation frequency and $\Delta f$ is the frequency sweep. To consider the phase shift of the received signal, the beat signal can be derived delaying the transmitted signal by the round-trip time $t_R$ as follows:

$$b_2(t) = \cos[2\pi f(t) t - 2\pi f(t)(t - t_R)] \tag{13}$$

Using (11), (13) becomes:

$$b_2(t) = \cos[2\pi f_0 t_R + 2\pi \Delta f f_m t_R t] \tag{14}$$

where $2\pi f_0 t_R$ is a phase shift term. For the time-domain modeling of all contributions in an array antenna (14) must be employed, as the above-mentioned phase term is essential to obtain a correct description of the wave propagation.

For a static target, the beat frequency is only due to the range and is the same for both $b_1$ and $b_2$:

$$f_R = \Delta f f_m t_R \tag{15}$$

Since $t_R = \frac{2R}{c_0}$, the range associated to the beat frequency $f_R$ is given by:

$$R = \frac{f_R c_0}{2 \Delta f f_m}. \tag{16}$$

When a power $P_T$ is transmitted by an antenna with gain $G_T$, the surface power density at the $i$-th target is:

$$\left.\frac{dP_i}{dS}\right|_{TX} = \frac{P_T G_T}{4\pi R_i^2}. \tag{17}$$

The surface power density at the radar receiver, backscattered from the target to the radar, is linearly dependent of the target RCS $\sigma_i$:

$$\left.\frac{dP_i}{dS}\right|_{RX} = \left.\frac{dP_i}{dS}\right|_{TX} \cdot \frac{\sigma_i}{4\pi R_i^2} = \frac{\sigma_i P_T G_T}{(4\pi)^2 R_i^4}, \tag{18}$$

The received power is obtained as follows:

$$P_{S_i} = \left.\frac{dP_i}{dS}\right|_{RX} \cdot A_{eff}, \tag{19}$$

where $A_{eff}$ is the receiving antenna effective area, related to the gain by the formula:

$$A_{eff} = \frac{G_R \lambda_0^2}{4\pi}. \tag{20}$$

Combining (19) and (20), the backscattered power from the target $i$ is therefore given by:

$$P_{S_i} = \frac{\sigma_i P_T G_T D_R \lambda_0^2}{(4\pi)^3 R_i^4 L_A}. \tag{21}$$

where the receiving antenna gain $G_R$ is expressed as the ratio between the receiving antenna directivity $D_R$ and the antenna loss $L_A$. By also including the low noise amplifier gain $G_{LNA}$ and the atmospheric loss $L_{ATM}$ we finally obtain the expression:

$$P_{S_i} = \frac{\sigma_i P_T G_T G_{LNA} D_R \lambda_0^2}{(4\pi)^3 R_i^4 L_A L_{ATM}}. \tag{22}$$

The coupling power between the transmitting and the receiving antenna, placed at a distance $l$ from one another, can be modeled as follows:

$$P_c = \frac{P_{Tx} G_{Tx} G_{LNA}}{\left(\frac{4\pi l}{\lambda_0}\right)^2} \frac{D_{Rx}}{L_A} SLL_{TX} SLL_{RX}, \tag{23}$$

where $SLL_{TX}$ and $SLL_{RX}$ are the end-fire transmitting and receiving antenna sidelobe level respectively. Finally, the time-domain beat signal can be written, according to (13), keeping into account the backscattered power from each target and the desired array excitation:

$$\begin{aligned} b_R(t) = &= \frac{1}{2}\sqrt{2P_C} \cos[2\pi(f(t) - f(t - \tau)]t \\ &+ \sum_{i=1}^{M} \sum_{j=1}^{N} \sum_{k=1}^{N} A_j A_k \sqrt{2\frac{P_{s_i}}{N}} \cos\{2\pi f(t) t \\ &+ -2\pi f(t)\left[t - t_{r_{ij}} - t_{r_{ik}} - t_{delay_j} - t_{delay_k}\right]\} \\ &+ awgn(t) \end{aligned} \tag{24}$$

where:
- $A_j$ is the $j$-th excitation coefficient, given by the array excitation;

- $t_{delay_j}$ is the delay associated to the propagation in the antenna BFN;
- $t_{r_{ij}}$ is the delay associated to the free-space propagation along the path $P_{ij}$;
- $awgn(t)$ is a time-domain signal associated to the system noise (see the following discussion for a quantitative description);
- $\tau = l/c_0$ is the delay applied to the transmitted chirp to model the coupling signal.

Since the delay associated to the propagation in the antenna BFN is affected by the wave velocity of the transmission line adopted to feed each radiator, if a dispersive waveguide is employed then the phase velocity $v_p(t)$ depends on the instantaneous frequency of the signal, and therefore the parameter $t_{delay_j}$ in (24) is time dependent and is defined as:

$$t_{delay_j} = \frac{(j-1)\, n \lambda_{g0}}{v_p(t)}, \tag{25}$$

The BFN in the presented antennas are based on SIW technology [23], [24], [25], with equivalent rectangular waveguide width $a_{eq}$. In this specific case the phase velocity can be therefore obtained as follows:

$$v_p = \frac{2\pi f}{\beta} = \frac{c}{\sqrt{1 - \left(\frac{\omega_c}{\omega}\right)^2}}. \tag{26}$$

with $c$ being the speed of light in the medium, equal to $c_0/\sqrt{\varepsilon_r}$, and the $TE_{10}$ propagation constant $\beta$ being:

$$\beta = \sqrt{\omega^2 \varepsilon_0 \varepsilon_r \mu_0 - \left(\frac{\pi}{a_{eq}}\right)^2} \tag{27}$$

As already mentioned, the system noise is also accounted in the formulation [26]. An additive white Gaussian noise (AWGN) is assumed, with total power expressed by the well-known formula:

$$N = k_B B T_{SYS}, \tag{28}$$

where $k_B$ is the Boltzmann's constant, $B$ is the band-pass filter bandwidth and $T_{SYS}$ is the system temperature. The total noise figure of the receiving chain, for a bistatic radar system as shown in Figure 20, is derived according to the Friis formula for noise:

$$F_{tot} = L_A + (F_{LNA} - 1)\, L_A + (L_{MIX} - 1)\, \frac{L_A}{G_{LNA}}, \tag{29}$$

The receiving chain input equivalent noise temperature is:

$$T_{eq} = T_0 (F_{tot} - 1), \tag{30}$$

The output total noise temperature is therefore obtained as:

$$T_{out} = G_{TOT} (T_A + T_{eq}) = \frac{G_{LNA}}{L_A L_{MIX}} (T_A + T_{eq}), \tag{31}$$

where $T_A$ is the antenna noise temperature. Substituting (30) in (31) we obtain:

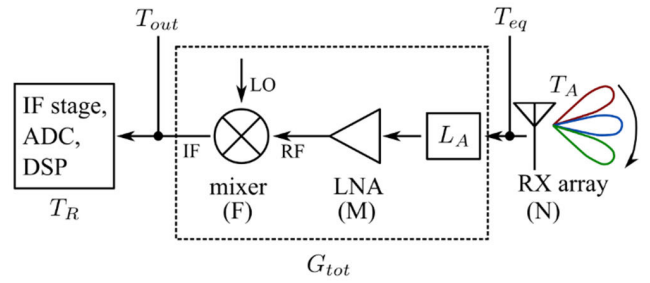$$T_{out} = \frac{G_{LNA}}{L_A L_{MIX}} [T_A + T_0 (F_{tot} - 1)]. \tag{32}$$



**FIGURE 20.** Homodyne radar receiver: block diagram.

The system noise temperature is finally obtained as follows:

$$T_{sys} = T_{out} + T_R$$
$$= \frac{G_{LNA}}{L_A L_{MIX}} [T_A + T_0 (F_{tot} - 1)] + T_0 (F_R - 1) \tag{33}$$

where $T_R$ is the receiver noise temperature.

The signal $awgn(t)$ is numerically generated as a uniformly distributed random sequence of samples properly scaled in amplitude according to the noise power level $N$.

## APPENDIX B
## MAPPING OF RADAR IMAGE ON RIVER SURFACE

With reference to Figure 21, we can assume the river to be flowing along the $y$ axis, and laying on the plane $x$-$y$, where the $xyz$ is the river reference system. The radar, whose reference system is $x'y'z'$, is assumed at a height $H$ from the river surface and rotated about $x$ axis by an angle $\alpha$, so that its broadside direction is oriented along $y'$ axis.
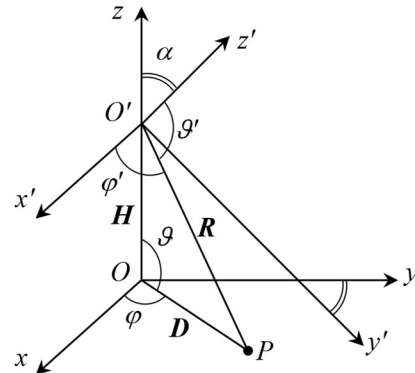


**FIGURE 21.** Radar and river reverence systems.

With these assumptions, the two above mentioned reference systems are related by the following equations:

$$\bar{x}_0 = \bar{x}'_0 \tag{34}$$
$$\bar{y}_0 = \bar{y}'_0 \cos a + \bar{z}'_0 \sin a \tag{35}$$
$$\bar{z}_0 = \bar{z}'_0 \cos a - \bar{y}'_0 \sin a \tag{36}$$

Let us consider a generic point $P$ over the river surface at a distance $D$ with respect to the river reference system origin $O$, or equivalently at a distance $R$ with respect to the radar reference system origin $O'$. Since the point $P$ is located on

the plane $z = 0$, the angle $\vartheta$ is equal to $\pi/2$ and $OPO'$ is a right triangle. The following relation therefore holds:

$$R^2 = H^2 + D^2 \tag{37}$$

and the coordinates of the point $P$ can be expressed as:

$$\begin{aligned}\bar{P} &= \sqrt{R^2 - H^2}\left(\cos\varphi\bar{x}_0 + \sin\varphi\bar{y}_0\right)\\ &= R\left(\sin\vartheta'\cos\varphi'\bar{x}_0' + \sin\vartheta'\sin\varphi'\bar{y}_0' + \cos\vartheta'\bar{z}_0'\right)\end{aligned} \tag{38}$$

From (34) and (38) we obtain:

$$\sqrt{R^2 - H^2}\cos\varphi = R\sin\vartheta'\cos\varphi' \tag{39}$$

Similarly, from equation (36) and (38) it results that:

$$0 = R\left(\cos\vartheta'\cos\alpha - \sin\vartheta'\sin\varphi'\sin\alpha\right) \tag{40}$$

From (40) we can derive the following expression for $\sin\vartheta'$:

$$\sin\vartheta' = 1\bigg/\sqrt{1 + \sin^2\varphi'\tan^2\alpha} \tag{41}$$

By substituting (41) in (39) we finally obtain:

$$\varphi = \cos^{-1}\left(\frac{R\cos\varphi'}{\sqrt{\left(R^2 - H^2\right)\left(1 + \sin^2\varphi'\tan^2\alpha\right)}}\right) \tag{42}$$

In this way, once the parameters $H$ and $\alpha$ are defined, by substituting (42) in (38) for each point $(R, \varphi')$ of the radar image the corresponding point $(D, \varphi)$ of the projected radar image can be obtained:

$$\begin{aligned}\bar{P} = &\frac{1}{\sqrt{1 + \sin^2\varphi'\tan^2\alpha}}\\ &\cdot\cdot\left(R\cos\varphi'\bar{x}_0\right.\\ &\left.+ \sqrt{\left(R^2 - H^2\right)\left(1 + \sin^2\varphi'\tan^2\alpha\right) - R^2\cos^2\varphi'}\,\bar{y}_0\right)\end{aligned} \tag{43}$$

## REFERENCES

[1] F. Bahmanpouri, S. Barbetta, C. Gualtieri, M. Ianniruberto, N. Filizola, D. Termini, and T. Moramarco, "Prediction of river discharges at confluences based on entropy theory and surface-velocity measurements," *J. Hydrol.*, vol. 606, Mar. 2022, Art. no. 127404, doi: 10.1016/j.jhydrol.2021.127404.

[2] Z. Wu, Y. Huang, K. Huang, K. Yan, and H. Chen, "A review of non-contact water level measurement based on computer vision and radar technology," *Water*, vol. 15, no. 18, p. 3233, Sep. 2023, doi: 10.3390/w15183233.

[3] T. Moramarco, S. Barbetta, D. M. Bjerklie, J. W. Fulton, and A. Tarpanelli, "River bathymetry estimate and discharge assessment from remote sensing," *Water Resour. Res.*, vol. 55, no. 8, pp. 6692–6711, Aug. 2019, doi: 10.1029/2018wr024220.

[4] F. Alimenti, S. Bonafoni, E. Gallo, V. Palazzi, R. V. Gatti, P. Mezzanotte, L. Roselli, D. Zito, S. Barbetta, C. Corradini, D. Termini, and T. Moramarco, "Noncontact measurement of river surface velocity and discharge estimation with a low-cost Doppler radar sensor," *IEEE Trans. Geosci. Remote Sens.*, vol. 58, no. 7, pp. 5195–5207, Jul. 2020, doi: 10.1109/TGRS.2020.2974185.

[5] Infineon Technologies. *77/79 GHz Automotive Radar Sensor ICS: Driver Assistance Systems*. Accessed: Sep. 7, 2023. [Online]. Available: https://www.infineon.com/cms/en/product/sensor/radar-sensors/radar-sensors-for-automotive/77-79ghz-radar/

[6] Texas Instruments. *Millimeter-Wave Radar Sensors Overview*. Accessed: Sep. 7, 2023. [Online]. Available: https://www.ti.com/sensors/mmwave-radar/overview.html

[7] D. Schwarz, N. Riese, I. Dorsch, and C. Waldschmidt, "System performance of a 79 GHz high-resolution 4D imaging MIMO radar with 1728 virtual channels," *IEEE J. Microw.*, vol. 2, no. 4, pp. 637–647, Oct. 2022, doi: 10.1109/JMW.2022.3196454.

[8] G. Ludeno, I. Catapano, F. Soldovieri, and G. Gennarelli, "Retrieval of sea surface currents and directional wave spectra by 24 GHz FMCW MIMO radar," *IEEE Trans. Geosci. Remote Sens.*, vol. 61, 2023, Art. no. 5100713, doi: 10.1109/TGRS.2023.3236359.

[9] M. A. Mutschler, P. A. Scharf, P. Rippl, T. Gessler, T. Walter, and C. Waldschmidt, "River surface analysis and characterization using FMCW radar," *IEEE J. Sel. Topics Appl. Earth Observ. Remote Sens.*, vol. 15, pp. 2493–2502, 2022, doi: 10.1109/JSTARS.2022.3157469.

[10] C. Fulton, M. Yeary, D. Thompson, J. Lake, and A. Mitchell, "Digital phased arrays: Challenges and opportunities," *Proc. IEEE*, vol. 104, no. 3, pp. 487–503, Mar. 2016, doi: 10.1109/JPROC.2015.2501804.

[11] R. D. Palmer, M. B. Yeary, D. Schvartzman, J. L. Salazar-Cerreno, C. Fulton, M. McCord, B. Cheong, D. Bodine, P. Kirstetter, H. H. Sigmarsson, T.-Y. Yu, D. Zrnić, R. Kelley, J. Meier, and M. Herndon, "Horus—A fully digital polarimetric phased array radar for next-generation weather observations," *IEEE Trans. Radar Syst.*, vol. 1, pp. 96–117, 2023, doi: 10.1109/TRS.2023.3280033.

[12] W. Mayer, M. Wetzel, and W. Menzel, "A novel direct-imaging radar sensor with frequency scanned antenna," in *IEEE MTT-S Int. Microw. Symp. Dig.*, Philadelphia, PA, USA, Aug. 2003, pp. 1941–1944, doi: 10.1109/MWSYM.2003.1210538.

[13] C. Vázquez, S. V. Hoeye, M. Fernandez, L. F. Herran, and F. L. Heras, "Frequency scanning probe for microwave imaging," in *Proc. IEEE Antennas Propag. Soc. Int. Symp.*, Toronto, ON, Canada, Jul. 2010, pp. 1–4, doi: 10.1109/APS.2010.5562108.

[14] Y. Alvarez-Lopez, C. Garcia-Gonzalez, C. Vazquez-Antuna, S. Ver-Hoeye, and F. Las-Heras, "Frequency scanning based radar system," *Prog. Electromagn. Res.*, vol. 132, pp. 275–296, 2012, doi: 10.2528/pier12071811.

[15] A. Shoykhetbrod, A. Hommes, and N. Pohl, "A scanning FMCW-radar system for the detection of fast moving objects," in *Proc. Int. Radar Conf.*, Lille, France, Oct. 2014, pp. 1–5, doi: 10.1109/RADAR.2014.7060388.

[16] T. Geibig, A. Shoykhetbrod, A. Hommes, R. Herschel, and N. Pohl, "Compact 3D imaging radar based on FMCW driven frequency-scanning antennas," in *Proc. IEEE Radar Conf. (RadarConf)*, Philadelphia, PA, USA, May 2016, pp. 1–5, doi: 10.1109/RADAR.2016.7485168.

[17] S. Li and S. Wu, "Low-cost millimeter wave frequency scanning based synthesis aperture imaging system for concealed weapon detection," *IEEE Trans. Microw. Theory Techn.*, vol. 70, no. 7, pp. 3688–3699, Jul. 2022, doi: 10.1109/TMTT.2022.3176404.

[18] *SWAN Software*. Accessed: Jun. 18, 2024. [Online]. Available: https://www.swan-soft.com

[19] G. Cicioni, G. Orecchini, R. V. Gatti, C. Saltalippi, V. Palazzi, P. Mezzanotte, L. Roselli, and F. Alimenti, "Frequency scanning surface velocity radar for river monitoring," in *IEEE MTT-S Int. Microw. Symp. Dig.*, San Diego, CA, USA, Jun. 2023, pp. 807–810, doi: 10.1109/ims37964.2023.10188189.

[20] S. Drabowitch, A. Papiernik, H. D. Griffiths, J. Encinas, and B. L. Smith, "Arrays," in *Modern Antennas*, 2nd ed. Dordrecht, The Netherlands: Springer, 2005, pp. 430–432.

[21] P. M. Relph and H. D. Griffiths, "An electronically scanning antenna for automotive radar systems," in *Proc. IEE Colloq. Automot. Radar Navigat. Techn.*, Sep. 1998, pp. 7-1–7-7, doi: 10.1049/ic:19980193.

[22] H. Rohling and C. Moller, "Radar waveform for automotive radar systems and applications," in *Proc. IEEE Radar Conf.*, Rome, Italy, May 2008, pp. 1–4, doi: 10.1109/RADAR.2008.4721121.

[23] X.-P. Chen and K. Wu, "Substrate integrated waveguide cross-coupled filter with negative coupling structure," *IEEE Trans. Microw. Theory Techn.*, vol. 56, no. 1, pp. 142–149, Jan. 2008, doi: 10.1109/TMTT.2007.912222.

[24] M. Pasian, M. Bozzi, and L. Perregrini, "Radiation losses in substrate integrated waveguides: A semi-analytical approach for a quantitative determination," in *IEEE MTT-S Int. Microw. Symp. Dig.*, Seattle, WA, USA, Jun. 2013, pp. 1–3, doi: 10.1109/MWSYM.2013.6697593.

[25] M. Pasian, M. Bozzi, and L. Perregrini, "Crosstalk in substrate integrated waveguides: A semi-analytical approach based on side leakage," in *Proc. 44th Eur. Microw. Conf.*, Rome, Italy, Oct. 2014, pp. 33–36, doi: 10.1109/EuMC.2014.6986362.

[26] M. Jankiraman, "Noise in radar receivers," in *FMCW Radar Design*, Norwood, CA, USA: Artech House, 2018, pp. 67–85.

**ROBERTO VINCENTI GATTI** (Member, IEEE) received the Laurea (magna cum laude) and Ph.D. degrees from the University of Perugia, Italy, in 2000 and 2007, respectively. Since 2007, he has been an Assistant Professor with the University of Perugia, where he currently teaches courses on antennas and wireless systems. Over the years he headed several industrial and research projects attaining a profound know-how and experience in the area of phased array antennas and RF passive microwave systems. He has produced more than 110 publications and presentations at international conferences. He holds two international patents and has developed a rigorous and efficient CAD tool for the analysis and design of large electronically scanning slotted waveguide antennas. His current research interests include the analysis, modeling, and design of phased arrays and reflectarrays, phase-only and phase/amplitude synthesis and optimization techniques for planar and conformal arrays, design of passive microwave and millimeter-wave components, and investigation of innovative architectures for reconfigurable devices. He is serving as a Reviewer for numerous technical journals, such as IEEE Transactions on Microwave Theory and Techniques, IEEE Transactions on Antennas and Propagation, *Electronics Letters* (IET Journals), *International Journal of Microwave and Wireless Technologies*, IEEE Transactions on Vehicular Technology, and *International Journal on RF and Microwave Computer-Aided Engineering*. Since 2009, he has been a member of the IEEE International Microwave Symposium (IMS) Technical Program Review Committee (TPRC), currently serving in "Airborne and Space Systems" Sub-Committee. He was appointed as the Chair of the IEEE IMS TPRC "Phased Arrays, MIMO and Beamformers" Sub-Committee, in November 2017, and the IEEE IMS TPRC "Airborne and Space Systems" Sub-Committee, in October 2022.

**GIORDANO CICIONI** (Graduate Student Member, IEEE) received the B.Sc. and M.Sc. degrees (magna cum laude) in electronic engineering from the University of Perugia, Perugia, Italy, in 2017 and 2020, respectively, where he is currently pursuing the Ph.D. degree in industrial and information engineering with the High-Frequency Electronics Laboratory. During the Ph.D. studies, he was a Visiting Researcher with the Institute für Mikrowellentechnik, Universität Ulm, Germany. His current research interests include the design and deployment of radar sensors for river monitoring applications. He was a recipient of the Second Place at the 3 Minute Thesis Competition held at IMS 2023.

**ALESSANDRO SPIGARELLI** received the master's degree (summa cum laude) in electronics and telecommunications engineering from the University of Perugia, Italy, in 2018. His academic pursuits have been primarily focused on the modeling, simulation, and design of FMCW radar architectures based on frequency steering phase array antennas, and the design of microwave passive components. In 2019, he joined Leonardo S.p.A. as a Radar System Engineer, contributing to the development of the surveillance Gabbiano radar system. He is currently a System Engineer at Elettronica S.p.A., specializing in the GCAP/Tempest product line.
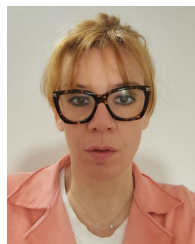
**GIULIA ORECCHINI** (Member, IEEE) received the Laurea degree in electronic engineering and the Ph.D. degree in electronic and information engineering from the University of Perugia, Italy, in 2008 and 2012, respectively. During the Ph.D. studies, she joined the ATHENA Research Group, Georgia Institute of Technology, Atlanta, GA, USA. She is currently a Researcher with the University of Perugia. Her main research interests include the development of radio-frequency identification systems and mm-wave transceivers for Cubesats applications.

**CARLA SALTALIPPI** received the Laurea degree (magna cum laude) in civil engineering from the University of Perugia, Italy, in 1995, and the Ph.D. degree in civil engineering from the University of Pavia, Italy, in 1999. Since 1999, she has been with the Department of Civil and Environmental Engineering, University of Perugia, initially as an Assistant Professor and now as an Associate Professor of hydrology, where she became a Full Professor, in 2021. She has authored more than 60 papers in journals/conference proceedings and books. The H-index of 20 with more than 1200 citations (source Scopus). Her research interests include real-time flood forecasting, rainfall-runoff modeling, infiltration modeling, rainfall characteristics, and open channel flow. Since 2019, she has been an Associate Editor of *Journal of Hydrology* (Elsevier).

**FEDERICO ALIMENTI** (Senior Member, IEEE) received the Laurea degree (magna cum laude) and the Ph.D. degree in electronic engineering from the University of Perugia, Italy, in 1993 and 1997, respectively. He was a Visiting Scientist with the Technical University of Munich, Germany. Since 2001, he has been with the Department of Engineering, University of Perugia, teaching the class of RFIC design. From 2011 to 2014, he was the Scientific Coordinator of the ENIAC ARTEMOS Project. In Summer 2014, he was a Visiting Professor with EPFL, Switzerland. He has participated at the Summer School 2017, held at Infineon Austria AG, Villach, as a Keynote lecturer. He has authored several patents and more than 200 papers in journals/conferences and books. The H-index of 26 with more than 2600 citations (source Scopus). His research interests include microwaves and RFIC design. In 1996, he was a recipient of the URSI Young Scientist Award. In 2013, he was also a recipient of the IET Premium (Best Paper) Award and the TPC Chair of the IEEE Wireless Power Transfer Conference. In 2018, he got the qualification as a "Full Professor" and won the "Mario Sannino" Award for the best research in the field of microwave electronics.

• • •